

Two-dimensional treatment of the level shift and decay rate in photonic crystals

D. P. Fussell,* R. C. McPhedran, and C. Martijn de Sterke

Center for Ultrahigh Bandwidth Devices for Optical Systems and School of Physics, University of Sydney, Sydney, NSW 2006, Australia

(Received 2 February 2005; revised manuscript received 12 April 2005; published 10 October 2005)

We present a comprehensive treatment of the level shift and decay rate of a model line source in a two-dimensional photonic crystal (2D PC) composed of circular cylinders. The quantities in this strictly two-dimensional system are determined by the two-dimensional local density of states (2D LDOS), which we compute using Rayleigh-multipole methods. We extend the critical point analysis that is traditionally applied to the 2D DOS (or decay rate) to the level shift. With this, we unify the crucial quantity for experiment—the 2D LDOS in a finite PC—with the band structure and the 2D DOS, 2D LDOS, and level shift in infinite PC's. Consistent with critical point analysis, large variations in the level shift are associated with large variations in the 2D DOS (and 2D LDOS), corroborating a giant anomalous Lamb shift. The boundary of a finite 2D PC can produce resonances that cause the 2D LDOS in a finite 2D PC to differ markedly from the 2D LDOS in an infinite 2D PC.

DOI: [10.1103/PhysRevE.72.046605](https://doi.org/10.1103/PhysRevE.72.046605)

PACS number(s): 42.70.Qs, 32.80.-t, 42.50.Dv

I. INTRODUCTION

Photonic crystals (PC's) were originally proposed by Yablonoivitch [1] and John [2], and are now a major field of research. The periodic dielectric function of a PC yields a photonic band structure with photonic band gaps, analogous to the electronic band structure in a crystal lattice [3]. The first proposed application of PC's was to inhibit spontaneous emission by suppressing the density of states (DOS) in a band gap and thereby reduce the threshold of a laser [1]. The modification of the DOS in a band gap is radically different to the modification at a cavity resonance [4], providing a new paradigm for quantum electrodynamics (QED) [5–7].

The early predictions of novel radiation dynamics in PC's [6] were based on band-edge models for the DOS [5,7]. These models follow from static models of the dispersion at the *critical points* in the band structure [8]. However, the fundamental quantity that determines radiation dynamics is the spatially resolved or local density of states (LDOS) [9]. More accurate modeling requires the LDOS from a vectorial treatment of the electromagnetic problem in a real PC. The calculations of the LDOS performed to date have focused on infinite PC's. The plane-wave expansion method (PWEM) [10,11] was used to obtain the LDOS in the two-dimensional (2D) PC composed of cylinders [11,12], the 3D PC's with diamond and inverted opal structures [11,13,14], and the woodpile 3D PC [15]. cursory examinations of the LDOS led to the contention that the band-edge models were invalid and, thus, also the predictions of non-Markovian behavior [13] and large anomalous Lamb shift [16]. The computation of the actual radiation dynamics using the LDOS has since resolved the dispute, and both predictions appear to be correct [14,17]. We have recently used our Rayleigh-multipole method [18] to study the density of states functions in 2D PC's composed of cylinders [19]. Recognizing that the experiment is performed on finite-sized PC's, we have calcu-

lated the 2D LDOS (for a line source) [20] and the 3D LDOS [21] (point source) in a finite array of cylinders.

A full demonstration of QED in PC's requires the complete 3D band gap of a 3D PC. However, the strictly two-dimensional system composed of a line source in a 2D PC remains a useful model for examining radiation dynamics in a PC. The reduced dimensionality allows detailed numerical modeling to be performed on a desktop computer [19,20], offering a compromise between simple one-dimensional examples and computationally prohibitive three-dimensional examples. In this paper we extend our Rayleigh-multipole methods to the calculation of the 2D band structure in 2D PC's composed of cylinders. This allows us to accurately and efficiently compute the 2D LDOS (decay rate) and the corresponding level shift (the classical part of the Lamb shift) in an infinite 2D PC. Introducing the analytic expressions for the level shift at the critical points, along with the usual expressions for the 2D DOS, we reconcile both the 2D LDOS and the level shift with the band structure. Furthermore, we show how confinement effects in the 2D PC can give rise to values of the 2D LDOS and the level shift which are strongly enhanced compared with their values in vacuo. We also reconcile the 2D LDOS in an infinite PC with the 2D LDOS in a finite 2D PC. These combined results represent an essentially complete treatment, whereby the quantity most relevant to experiment—the LDOS in a finite PC—is tied to the band structure.

We begin in Sec. II by summarizing the basic theoretical aspects of the results: the determination of the decay rate and level shift by the LDOS and the expressions for the two-dimensional DOS and level shift at the critical points. In Sec. III, we connect the numerical 2D LDOS in infinite 2D PC's, and the level shift, to the band structure through critical point analysis and the Bloch functions. In Sec. IV, we connect the 2D LDOS in infinite and finite 2D PC's through the resonances of the 2D PC. Finally in Sec. V, we discuss the results and draw conclusions. In Appendix A, we briefly describe the adaption our Rayleigh-multipole method to the computation of the band structure in infinite 2D PC's and demonstrate that the accuracy of the method is limited only by

*Electronic address: fussell@physics.usyd.edu.au

machine precision. In Appendix B, we present an accurate and efficient method for calculating the 2D DOS and the 2D LDOS from the band structure.

II. THEORETICAL FRAMEWORK

A. Local density of states

The key quantity that determines the radiation dynamics in a structured dielectric environment, employing either perturbative or exact treatments [6,7,14,22], is the spatially resolved or local density of states [9]. The 3D LDOS applies to a real, randomly oriented, point like atom, while the 2D LDOS applies to a model line source. The 2D LDOS in an infinite 2D PC is defined as [11,19]

$$\rho(\mathbf{r}, \omega) = \frac{1}{A_{\text{BZ}}} \sum_l \int_{\text{BZ}} d^2 \mathbf{k}_0 |\Psi_l^E(\mathbf{k}_0, \mathbf{r})|^2 \delta(\omega - \omega_l(\mathbf{k}_0)), \quad (1)$$

where A_{BZ} is the area of the Brillouin zone (BZ) and $\Psi_l^E(\mathbf{k}_0, \mathbf{r})$ is the electric Bloch function at the Bloch vector \mathbf{k}_0 of the l th band surface.

In the Wigner-Weisskopf approximation (WWA), the LDOS allows the level shift $\Delta\omega$ and the decay rate Γ for a two-level atom to be written as [7]

$$\Delta\omega(\mathbf{r}, \omega) - i \frac{\Gamma}{2}(\mathbf{r}, \omega) = \frac{1}{\hbar^2} \frac{\hbar\omega}{2} \frac{\mu_{ab}^2}{\epsilon_0} \frac{1}{3} \left[\int_0^\infty d\omega' \frac{\omega}{\omega'} \frac{\rho(\mathbf{r}, \omega')}{\omega - \omega'} - i\pi\rho(\mathbf{r}, \omega) \right], \quad (2)$$

where μ_{ab} is the amplitude of the dipole transition matrix element. The WWA applies when the LDOS is a smooth function of frequency, in which case the radiation dynamics follows an exponential law with a decay rate and level shift proportional to the LDOS and its Hilbert transform, respectively. When the LDOS varies sharply, the radiation dynamics is nonexponential, but the LDOS and its Hilbert transform remain the key elements in the more general treatment [22].

The LDOS is the important quantity for PC's operating at optical wavelengths because the spatial variation in the refractive index, and hence the Bloch functions, occurs on scales of the order of 10^3 times greater than the size of an atom. While the spatially independent density of states is more commonly used in solid-state physics, in PC's it only applies to limited experiments where atoms are evenly distributed over the unit cell. However, it is more closely linked to the band structure than the LDOS and is thus useful for theory. In a 2D PC, the 2D DOS is defined as

$$N(\omega) = \sum_l \int_{\text{BZ}} d^2 \mathbf{k}_0 \delta(\omega - \omega_l(\mathbf{k}_0)). \quad (3)$$

When the Bloch functions are normalized according to

$$\int_{\mathcal{U}} d^2 \mathbf{r} n(\mathbf{r})^2 |\Psi_l^E(\mathbf{k}_0, \mathbf{r})|^2 = 1, \quad (4)$$

where $n(\mathbf{r})$ is the refractive index in the unit cell \mathcal{U} , the 2D DOS is related to the 2D LDOS by

$$N(\omega) = \int_{\mathcal{U}} d^2 \mathbf{r} n(\mathbf{r})^2 \rho(\omega, \mathbf{r}). \quad (5)$$

The 2D LDOS and 2D DOS can be simplified to contour integrals over the irreducible Brillouin zone (IBZ) [23]. The 2D LDOS becomes

$$\rho(\omega, \mathbf{r}) = \sum_{i=1}^{n_g} \sum_l \frac{1}{A_{\mathcal{U}}} \int_{C(\omega_l)} \frac{|\Psi_l^E(\mathbf{k}_0, \{\hat{\beta}_i\}^{-1} \mathbf{r})|^2}{v_g} dk_{0l}, \quad (6)$$

where $C(\omega_l)$ are the isofrequency contours that traverse the l th band surface over the IBZ, v_g is the group velocity on the contour, k_{0l} is the projection of the Bloch vector onto the contour, $A_{\mathcal{U}}$ is the area of the unit cell, and $\{\hat{\beta}_i\}$ are the n_g elements of the lattice point group. Similarly the 2D DOS becomes

$$N(\omega) = n_g \sum_l \frac{1}{A_{\mathcal{U}}} \int_{C(\omega_l)} \frac{1}{v_g} dk_{0l}. \quad (7)$$

We compute the band surfaces and Bloch functions required for the 2D DOS and 2D LDOS using the Rayleigh-multipole method, which is summarized in Appendix A. The method used to compute Eqs. (6) and (7) is then described in Appendix B. With the 2D LDOS and 2D DOS in hand, the associated level shift can be obtained by evaluating the Hilbert transform integral in Eq. (2) [24,25]. As we note in Appendixes A and B, and Ref. [24], all of these methods produce results to high accuracy. Note though that the level shift of a two-level atom amounts to considering only the classical part of the Lamb shift for a real multilevel atom. To maintain results that are general and independent of the atom and the radiation dynamics, neither the decay rate nor the level shift is evaluated explicitly. Rather, results are restricted to the two quantities in square brackets in Eq. (2): the LDOS and its Hilbert transform. However, we will refer to the Hilbert transform of the LDOS as the level shift.

B. Critical points

As is well known from solid-state physics [8,26–29], the significant variations in the DOS occur at the *critical points* in a band where $v_g=0$, producing *van Hove singularities* in the integrand of Eq. (7). In this paper we apply critical point analysis to the 2D DOS in 2D PC's and extend it to the level shift. At the minima (P_0) and maxima (P_2) of a two-dimensional band surface, the 2D DOS is a (positive or negative) discontinuity [8,28]

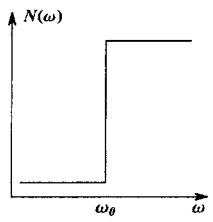
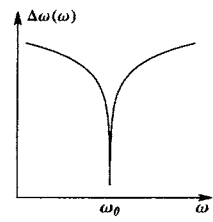
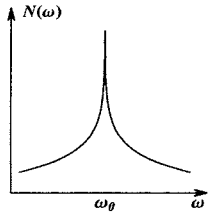
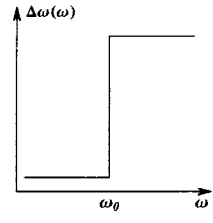
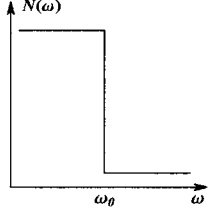
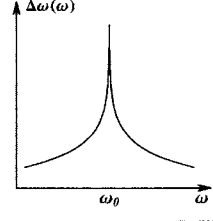
$$N(\omega) = \epsilon_{x,y} A H(\omega - \omega_0) + B, \quad (8)$$

where $\epsilon_{x,y} = \pm 1$ and $H(\omega)$ is the Heaviside step function with value 0 for $\omega < 0$ and 1 for $\omega > 0$. At the saddle points (P_1) of a band surface, the 2D DOS is a logarithmic singularity (with negative coefficient) [8,28]

$$N(\omega) = -A \ln|\omega - \omega_0| + B. \quad (9)$$

In both Eqs. (8) and (9), A is a positive constant, while B is a positive constant in Eq. (8) and arbitrary in Eq. (9), with all depending upon the particular band structure. In a 2D PC,

TABLE I. DOS and level shift at critical points. In the functions, $A=4\sqrt{C_x C_y}/A_{\text{WSC}}$ is a positive constant, B is arbitrary for P_1 and positive for P_0 and P_2 , and B' is arbitrary.

Critical Point	DOS [$N(\omega)$]		level shift [$\Delta\omega(\omega)$]	
	Function	Schematic	Schematic	Function
P_0 Minimum	$N(\omega) = A H[\omega - \omega_0] + B$			$\Delta\omega(\omega) = \frac{A}{\pi} \ln \omega - \omega_0 + B'$
P_1 Saddle	$N(\omega) = -A \ln \omega - \omega_0 + B$			$\Delta\omega(\omega) = \frac{A}{\pi} H[\omega - \omega_0] + B'$
P_2 Maximum	$N(\omega) = -A H[\omega - \omega_0] + B$			$\Delta\omega(\omega) = -\frac{A}{\pi} \ln \omega - \omega_0 + B'$

$A=4\sqrt{C_x C_y}/A_{\text{WSC}}$ [19] and it depends on the positive curvature parameters C_x and C_y , which are analogous to the effective mass in solid-state physics.

The level shift $\Delta\omega(\omega)$ is determined by the (negative) Hilbert transform of the DOS [see Eq. (2)]. The logarithmic singularity and step function are related by the Hilbert transform

$$\mathcal{H}[H(\omega)] \equiv \frac{1}{\pi} \int_{-\infty}^{\infty} \frac{H(\omega')}{\omega' - \omega} d\omega' = -\frac{1}{\pi} \ln |\omega|. \quad (10)$$

Over the narrow frequency range in the vicinity of a critical point, it is reasonable to assume in Eq. (2) that $\omega \approx \omega'$. At P_0 and P_2 , the level shift is then logarithmic singular,

$$\Delta\omega(\omega) = \epsilon_{x,y} \frac{A}{\pi} \ln |\omega - \omega_0| + B', \quad (11)$$

while at P_1 it is a discontinuity

$$\Delta\omega(\omega) = \frac{A}{\pi} H(\omega - \omega_0) + B', \quad (12)$$

where now B' is an arbitrary constant in both equations.

The functional forms of the 2D DOS and the level shift at the critical points are presented in Table I. The addition of the level shift to the familiar 2D DOS completes the picture for the radiative dynamics of a line source at the critical points. Note that there is an asymmetry between the 2D DOS and the level shift: as the DOS cannot be negative the 2D

DOS does not have a logarithmic singularity with a positive coefficient; there is thus a corresponding absence of a negative step function in the level shift. It is also important to qualify the critical point behavior when it is applied to experiment. Measurements are performed on samples that are finite and contain imperfections. Thus, in practice, while the LDOS or level shift may be sharply peaked or change abruptly, they can neither be singular nor discontinuous [8].

For each band, the number of critical points within the BZ is constrained by topology [27–29]. If a 2D band surface contains only analytic critical points, then there must be at least one minimum, except for the first band, one maximum, and two saddle points, though by symmetry the frequency of the saddle points may coincide [28]. At the band degeneracies of high-symmetry points, analyticity is only brought about by considering bands individually. The ordering of bands (see Appendix B) can also yield nonanalytic critical points at band crossings, which are required to be included in a more complicated topological argument [29].

III. INFINITE 2D PC's

In this section we examine the connection between the 2D band structure and the 2D LDOS, along with the corresponding level shift, in infinite 2D PC's. The 2D PC's are composed of an infinite array of cylinders arranged in a Cartesian coordinate system (Appendix A) with lattice constant d . We consider two 2D PC's. The first, the 2D macroporous silicon

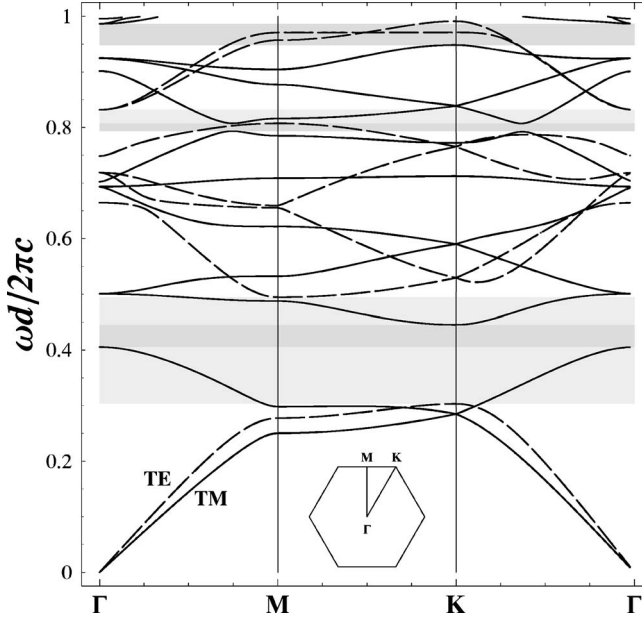


FIG. 1. Band structure for the 2D MSPC: hexagonal lattice with air-void radius $a/d=0.45$, air-void refractive index $n_l=1.0$, and background refractive index $n_b=3.4$. TM gaps: (1) $\omega d/2\pi c=0.405395-0.445216$, (2) $0.793405-0.807234$, and (3) $0.948340-0.986478$. TE gaps: (1) $0.303245-0.494463$ and (2) $0.807461-0.831659$.

PC (MSPC), is based on macroporous silicon [30] and is composed of a hexagonal lattice of cylindrical air voids with radius $a/d=0.45$ and refractive index $n_l=1.0$, in a background of refractive index $n_b=3.4$. The band structure is shown in Fig. 1. For each polarization there is a wide first-order gap at the normalized frequency $\omega d/2\pi c \sim 0.4$ and a narrow second-order gap at $\omega d/2\pi c \sim 0.8$, and the first-order TM gap lies wholly within the first-order TE gap to form a complete gap. Line plots of the 2D LDOS in the 2D MSPC are shown in Fig. 2. Also included for easy comparison are the 2D DOS and level shift, and each will be discussed in turn. The line plots cover the frequency range $\omega d/2\pi c=0.0-0.8$ with data points at $\omega d/2\pi c=0.0005p$, $p \in \mathbb{N}$. Density plots of the 2D LDOS in the unit cell are shown in Fig. 3. The second structure, the 2D square PC (SQPC), is a square lattice of dielectric cylinders with radius $a/d=0.30$ and refractive index $n_l=3.0$ in an air background with refractive index $n_b=1.0$. The band structure for the 2D SQPC is shown in Fig. 4 and has no TE gaps, but wide first- and second-order gaps for TM polarization. Line plots of the 2D LDOS and level shift are shown in Fig. 5, while the 2D LDOS in the unit cell is shown in Fig. 6.

A. 2D local density of states

The 2D DOS is well known (e.g., [11,19]), but is nonetheless a good starting point since it is more closely tied to the band structure than the 2D LDOS. The 2D DOS in the 2D MSPC is shown in Figs. 2(a) and 2(b) for TM and TE polarization, respectively, and in the 2D SQPC in Fig. 5(a) for TM polarization only. The significant features in the 2D

DOS are readily understood through critical point analysis (Table I). Close inspection shows that one degenerate pair of saddle points is contained within each band and contributes one logarithmic singularity to the 2D DOS. Furthermore, maxima at the top of each band contribute a discontinuity, as do minima at the bottom of all but the first band. Following from Table I, the heights of the discontinuities in the 2D DOS at the minima and maxima are determined by the band curvature parameters C_x and C_y . As we noted above, the plots are produced using equally spaced data points, so we sample near, but not precisely at, the saddle points. The logarithmic singularities are therefore truncated, and the height of the peaks in the 2D DOS at the saddle points are also determined by C_x and C_y . Note in the plots that the height of the peaks increases as we move into the flatter bands at higher frequencies.

The 2D LDOS is shown in Figs. 2 and 5 alongside the 2D DOS. These plots show the frequency dependence of the 2D LDOS at significant positions in the unit cell. The 2D LDOS in the unit cell of the 2D MSPC is shown in Fig. 3 and for the 2D SQPC in Fig. 6. These plots show the spatial dependence of the 2D LDOS at a selection of critical points. Analyzed in combination, both types of plots provide a broad picture of the behavior in the 2D LDOS. Note in Figs. 3 and 6 that following the summation over point group operations in Eq. (6), the 2D LDOS is invariant under point group operations.

In addition to the group velocity and contour length, the 2D LDOS [Eq. (7)] is determined by the field intensity in the Bloch function $|\Psi_l^E(\mathbf{k}_0, \mathbf{r})|^2$. The LDOS in general reflects the DOS scaled by the characteristic nodal pattern of the Bloch functions in each band and is low near nodes and high near antinodes. Band and Bloch function formation is governed by the electromagnetic variational theorem [3], by which modes concentrate their energy in the high dielectric region while remaining orthogonal to modes below in frequency. It is easiest to observe the consequences of this for TM polarization in the 2D SQPC where the field lines traverse a relatively uncomplicated dielectric structure. In the first band, Bloch functions minimize energy with an antinode at the center of the dielectric cylinder, where the 2D LDOS is accordingly maximum, and nodal planes in the background where the 2D LDOS is minimum [Fig. 6(a)]. Above the band gap in the second band, orthogonal modes are then formed with nodal planes running through the cylinder center, where the 2D LDOS is now minimum [Fig. 6(b)]. In the 2D MSPC, a similar result emerges for TE polarization, though with a dielectric background the 2D LDOS at the center of the air void is minimum in the first band and maximum in the second band [Figs. 3(e) and 3(f)]. For TM polarization, the first two bands are connected and the 2D LDOS is minimum at the air-void center for both bands [Fig. 3(a)]. Above the band gap in the third band, the 2D LDOS is then maximum at the air-void center [Fig. 3(b)]. Modes in higher bands form with more complicated nodal patterns, which manifest themselves in more complicated profiles for the 2D LDOS in the unit cell [see Figs. 3(c), 3(d), 6(c), and 6(d)].

The orthogonality of the modes in the two bands surrounding a band gap introduces an interesting distinction between the DOS and LDOS. The P_0 and P_2 points that form

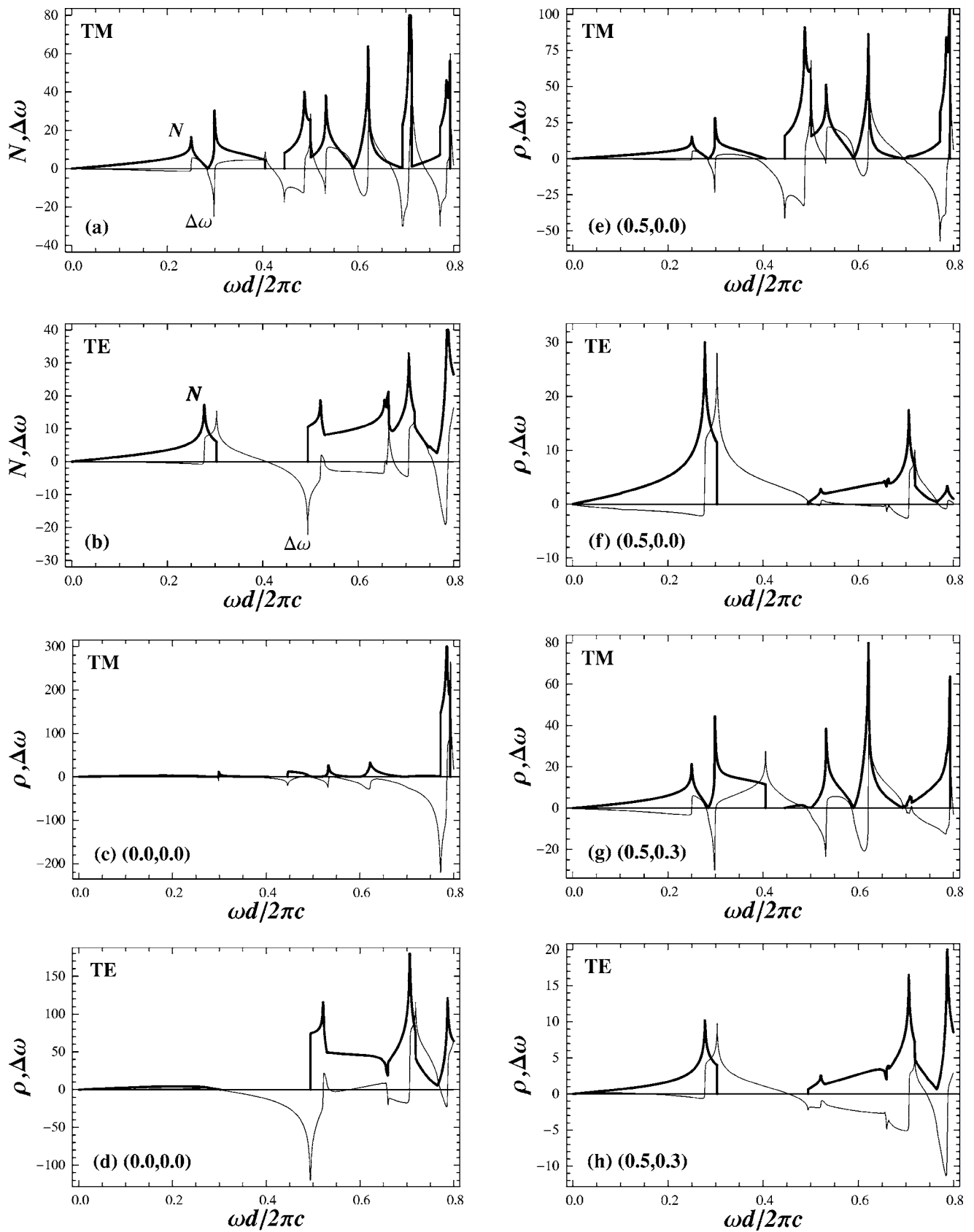


FIG. 2. 2D DOS N (a), (b) and 2D LDOS ρ (c)–(h) (thick-line) and corresponding level shift ($\Delta\omega$) (thin line) in the 2D MSPC. For the 2D LDOS (c), (d) $\mathbf{r}/d=(0.0,0.0)$; (e), (f) $\mathbf{r}/d=(0.5,0.0)$; and (g), (h) $\mathbf{r}/d=(0.5,0.3)$.

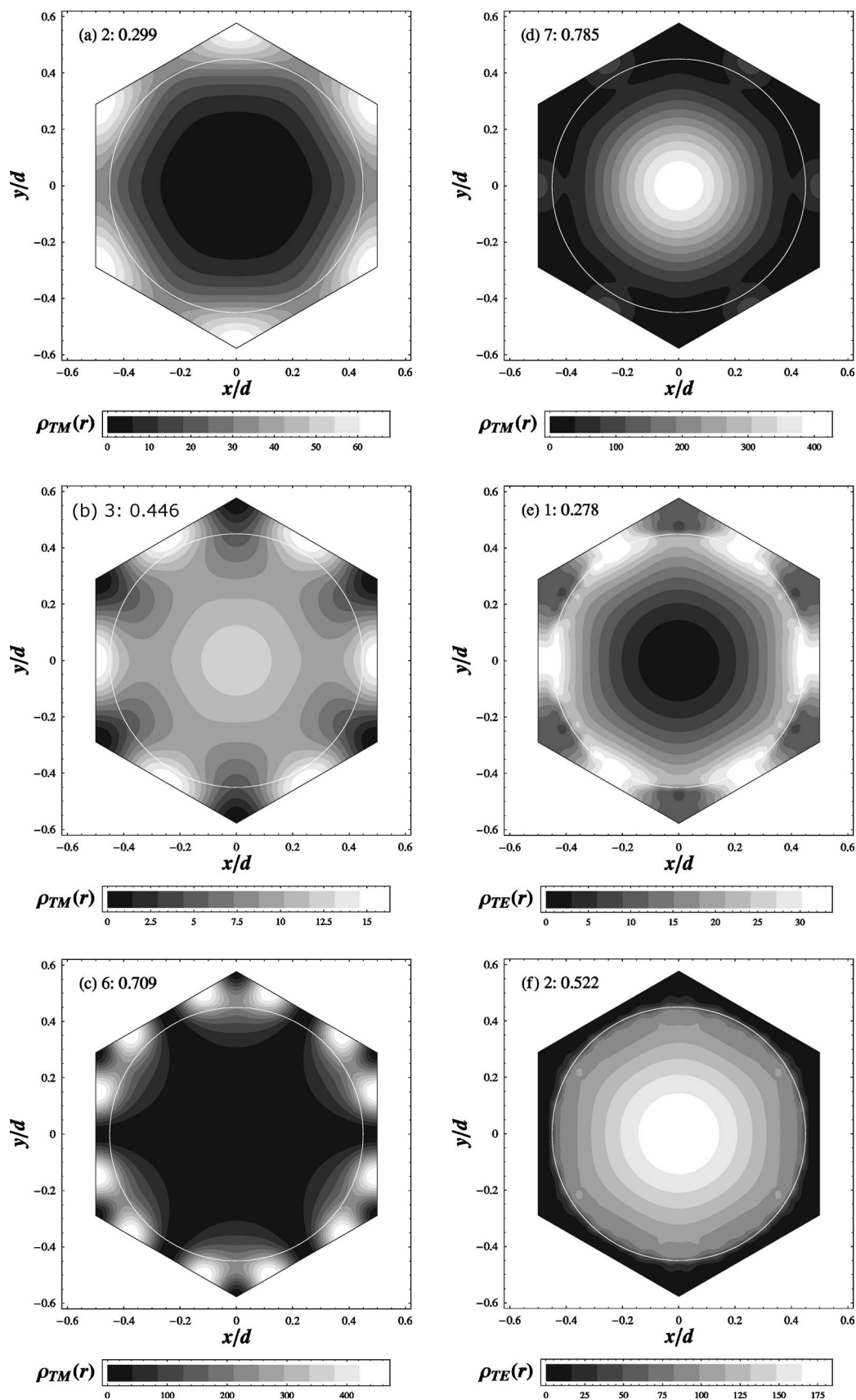


FIG. 3. 2D LDOS ρ at critical points in the 2D MSPC. TM polarization: (a) band 2, $\omega d/2\pi c=0.299$, P_1 critical point at M point in BZ; (b) band 3, 0.446, P_0 at K ; (c) band 6, 0.709, P_1 at M ; and (d) band 7, 0.785, P_1 at M . TE polarization: (e) band 1, 0.278, P_1 at M ; and (f) band 2, 0.522, P_1 .

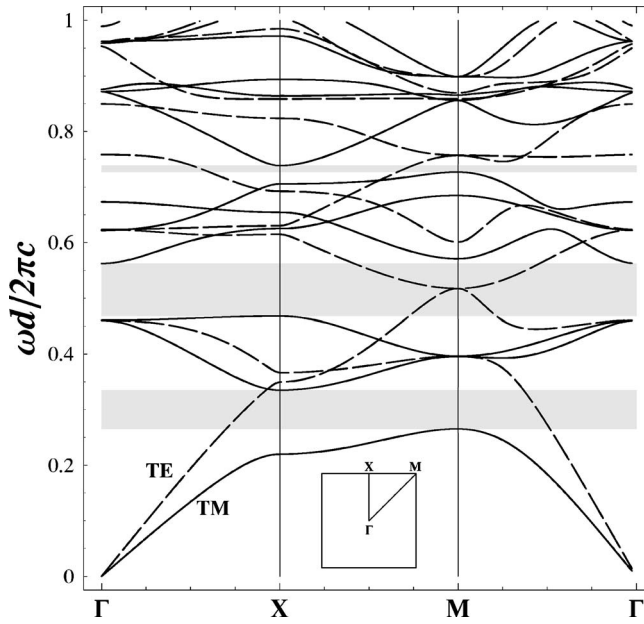


FIG. 4. Band structure for the 2D SQPC: square lattice with cylinder radius $a/d=0.30$, cylinders refractive index $n_i=3.0$, and background refractive index $n_b=1.0$. TM gaps: (1) $\omega d/2\pi c=0.265263-0.334947$, (2) $0.468027-0.562353$, and (3) $0.726880-0.738487$.

the edges of a band gap produce significant discontinuities in the 2D DOS. However, the positions of the nodes on one side of a band gap correspond to antinodes on the other. At these positions, the discontinuity is eliminated in the 2D LDOS on the nodal side of the band gap and is strengthened on the antinodal side. This can be seen clearly about the TE band gap of the 2D MSPC in Figs. 2(d) and 2(f) and about the TM band gap of the 2D SQPC in Figs. 5(b) and 5(c). At positions sufficiently displaced from the nodes and antinodes, the field intensity in the Bloch functions varies more moderately, and the 2D LDOS essentially replicates the 2D DOS [Fig. 5(d)].

At frequencies removed from the critical points, v_g varies moderately on an isofrequency contour so that all modes on the contour make a contribution to the 2D LDOS. As the nodal pattern generally rotates with the Bloch vector around a contour, the summation over all of these modes prevents large variations in the 2D LDOS in the unit cell, unless nodes or nodal planes run through the center of the unit cell. When a contour passes close to a critical point by contrast, v_g is smallest near the critical point, and the 2D LDOS is completely determined by the nodal pattern of the mode at this point [19]. In principle, the 2D LDOS at a saddle point is singular in the unit cell except at nodes. As we noted when discussing the 2D DOS, we sample near, but not precisely at, the saddle points. The 2D LDOS is thus largest, but not singular, near the antinodes of the saddle point modes in the flat bands. For TM polarization in the 2D MSPC, this occurs in the sixth band at $\omega d/2\pi c=0.785$ [Fig. 2(c)] at the center

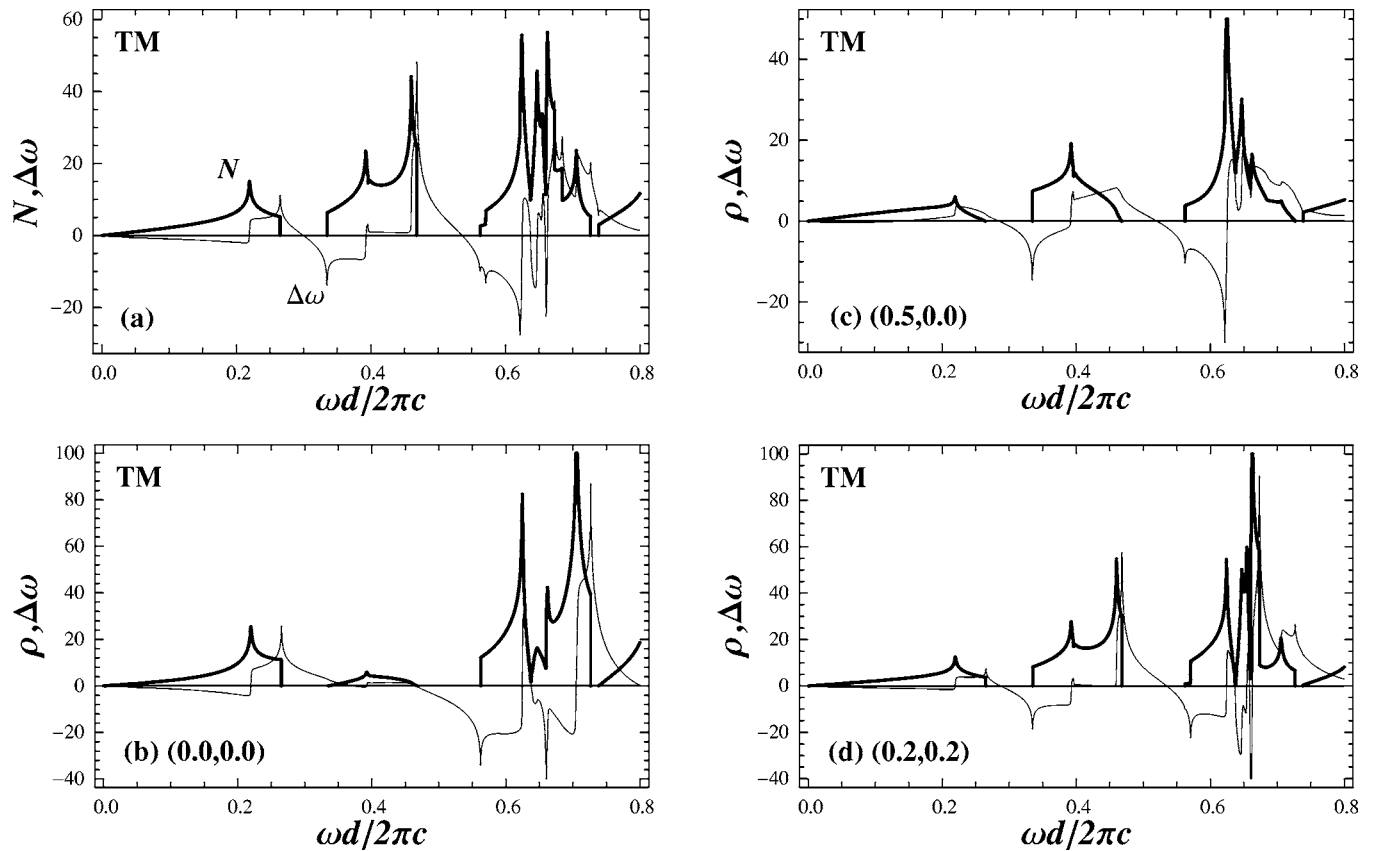


FIG. 5. 2D DOS N (a) and 2D LDOS ρ (b)–(d) (thick-line) and corresponding level shift ($\Delta\omega$) (thin line) for TM polarization in the 2D SQPC. For 2D LDOS (b) $\mathbf{r}/d=(0.0,0.0)$, (c) $\mathbf{r}/d=(0.5,0.0)$, and (d) $\mathbf{r}/d=(0.2,0.2)$.

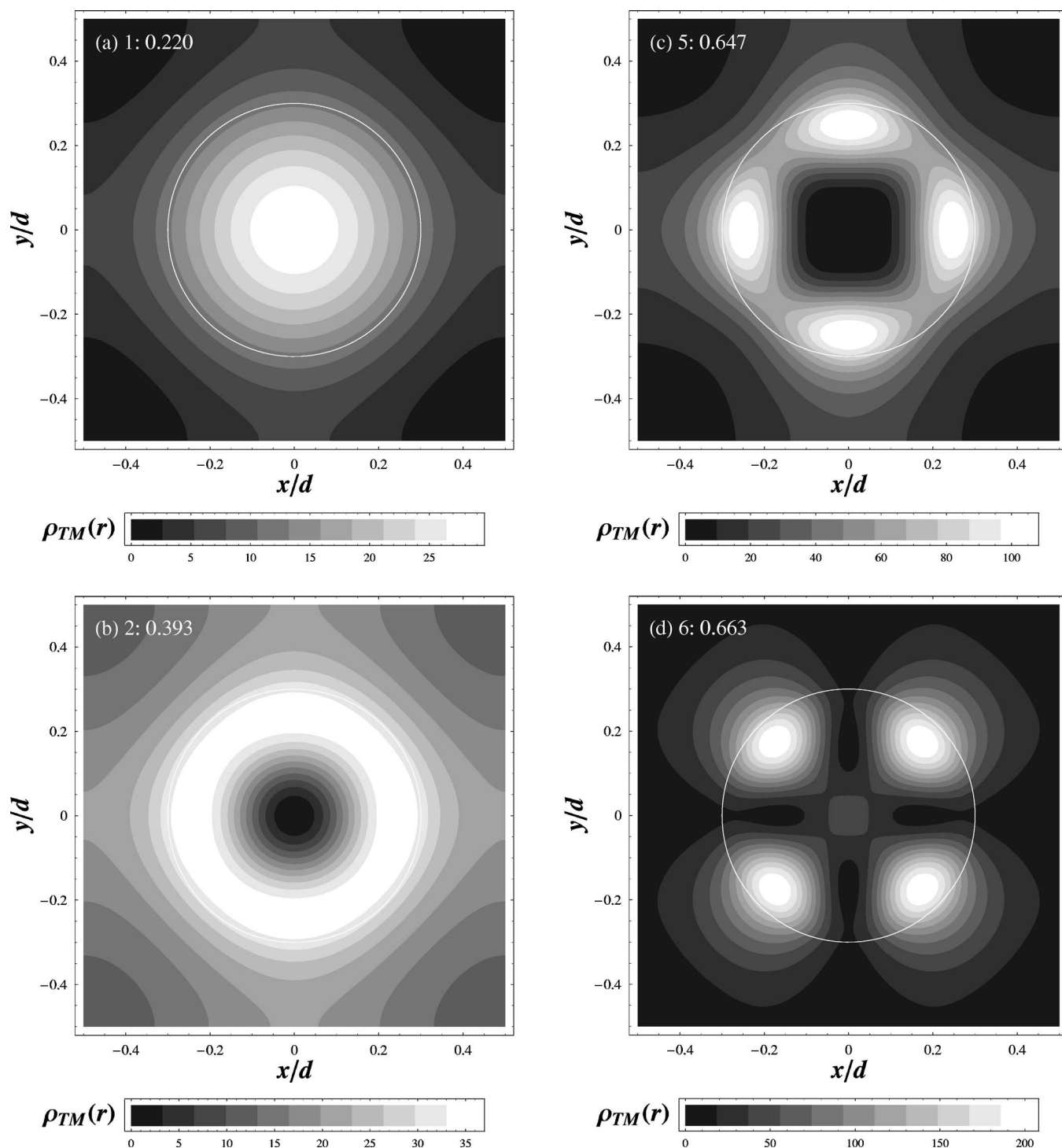


FIG. 6. 2D LDOS ρ at critical points in the 2D SQPC for TM polarization: (a) band 1, $\omega d/2\pi c=0.220$, P_1 critical point at the X point in BZ; (b) band 2, 0.393, P_1 ; (c) band 5, 0.647, P_1 ; and (d) band 6, 0.663, P_1 .

of the air void [Fig. 3(d)]. For TM polarization in the 2D SQPC, the 2D LDOS is largest in the sixth band at $\omega d/2\pi c=0.663$ [Fig. 5(d)] inside the cylinder surface [Fig. 6(d)].

B. 2D level shift

We examine the level shift ($\Delta\omega$) by evaluating [Eq. (2)]

$$\Delta\omega \sim \int_0^{\omega_c} d\omega' \frac{\omega}{\omega'} \frac{\rho(\mathbf{r}, \omega')}{(\omega - \omega')}, \quad (13)$$

where $\omega_c d/2\pi c=1$, extended a small amount beyond the range we examine for the 2D LDOS. While the results are produced to high accuracy [24], the complete computation of the level shift requires mass renormalization [7,31]

$$\Delta\omega(\mathbf{r}, \omega) \rightarrow \Delta\omega(\mathbf{r}, \omega) - \Delta\omega(\mathbf{r}, 0) = \int_0^{\omega_e} d\omega' \frac{\omega^2 \rho(\mathbf{r}, \omega')}{\omega'^2 (\omega' - \omega)}, \quad (14)$$

where ω_e is the Compton frequency. The mass renormalization diminishes the absolute value of the integral at low frequencies and enhances it at high frequencies. It also involves integration up to ω_e , which in practice is evaluated by approximating the integral in the range $\omega_c - \omega_e$ by the free-space result and increasing ω_c to a value at which the total result converges [17]. This has a small broadband effect and does not significantly alter the narrow-band effects of interest here.

The level shift is shown with the 2D DOS and LDOS in Fig. 2 for the 2D MSPC and in Fig. 5 for the 2D SQPC. As we use Eq. (13), it is not possible to quantify the result at low frequencies as has been done for the 2D DOS [19]. However, the ω factor in Eq. (13) ensures that $\Delta\omega \rightarrow 0$ as $\omega \rightarrow 0$, as is clear in the plots. At higher frequencies, all significant features in the level shift are consistent with critical point analysis (Table I). Note in Figs. 2 and 5 that the level shift varies on a similar scale to the 2D DOS and LDOS. From Table I, this is because the critical point behavior is determined by the same curvature parameters. Large upward jumps in the level shift are associated with pronounced logarithmic singularities in the 2D DOS (and LDOS), while pronounced peaks in the level shift are associated with large discontinuities in the 2D DOS (and LDOS) [e.g., Fig. 2(c)]. These large variations in the level shift are consistent with the prediction of a giant anomalous Lamb shift (GALS) in PC's [17]. As highlighted by Wang *et al.* [17], it was the spurious use of smooth approximations for the LDOS that led to the belief that the anomalous Lamb shift in PC's was negligible [16]. In a real multilevel atom, the strong frequency variation of the LDOS in PC's at optical wavelengths has a significant impact on real (as opposed to virtual) transitions, leading to a GALS two orders of magnitude greater than the vacuum Lamb shift [16].

The critical point behavior of the level shift also produces interesting results about a band gap. The significant discontinuities in the 2D DOS on the band-gap edges result in a positive peak in the level shift on the bottom edge and a negative peak on the top edge (again consistent with Table I). Thus, at both the bottom and top edges, the emission frequency is pushed into the band gap. This implies a “rounding” and “narrowing” of the observed spectral signature of the band gap. Furthermore, the level shift is forced to pass through zero inside the band gap [e.g., see Fig. 2(b)]. Both of these results were identified by Kofman, Kurizki, and Sherman [6]. However, the strong differences in the band-gap behavior between the 2D DOS and 2D LDOS noted above also have important consequences for the level shift. At the position of a node, where the discontinuity in the 2D LDOS is absent, there is no corresponding peak in the level shift. In this case, the spectral signature of the band gap is still diminished, but through the 2D LDOS rather than the level shift. Furthermore, the level shift passes through zero within the band occupied by the node rather than the band gap [e.g.,

Figs. 2(e) and 2(g)]. Note though [see, e.g., Fig. 2(h)] that only a small discontinuity in the 2D LDOS is required to produce a peak in the level shift, and the level shift is again forced through zero inside the band gap. This occurs at small displacements from the nodes.

IV. FINITE 2D PC'S

The dimensions of PC's fabricated at present are typically $\sim 10^2 - 10^3$ times the lattice constant. The finite size of these PC's has potentially significant effects. The 2D LDOS in the finite and infinite forms of the 2D PC's are compared in Fig. 7. The 2D LDOS in the finite 2D PC's is calculated using the Green tensor approach described in Ref. [20]. The finite 2D PC has the same unit cell as the corresponding infinite 2D PC, but is constructed from a finite number of N_c unit cells. The 2D LDOS in the 2D SQPC is shown in Figs. 7(a)–7(d) using two different-sized clusters. The first cluster [Fig. 7(a)] is composed of the $N_c = 101$ cylinders that fit wholly within a circular boundary of radius $6.0d$ and the second [Figs. 7(b)–7(d)] of the $N_c = 137$ cylinders within a boundary of radius $7.0d$. The clusters have an approximately circular boundary and are surrounded by an air background of infinite extent. The 2D LDOS in the 2D MSPC is shown in Figs. 7(e) and 7(f), and is composed of $N_c = 91$ air voids packed in five hexagonal rings of air voids about a central air void. This cluster has an approximately hexagonal boundary enclosed by a silicon boundary of infinite extent.

At the frequencies that we consider, the 2D SQPC cluster behaves like a single dielectric structure—an approximately circular dielectric waveguide in air. This structure has strong resonances with quality factors (Q 's) that increase with frequency or, equivalently, the waveguide radius [24]. At low frequencies, the effective index of the cluster is given by the linear mixing formula [32]. In Figs. 7(a) and 7(b) we indicate with vertical lines the location of the zeroth-order resonances for a circular dielectric waveguide with refractive index $n_{\text{eff}} = 1.806$ in air. The waveguide has radius $6.0d$ in Fig. 7(a) and $7.0d$ in Fig. 7(b). The zeroth-order resonances have antinodes at the waveguide center, which correspond reasonably well to the peaks in the 2D LDOS at low frequencies ($\omega d / 2\pi c < 0.2$). At higher frequencies, the effective index of the cluster is not easily quantifiable. However, sequences of equally spaced resonances are discernable [e.g., second and third bands in Figs. 7(c) and 7(d)], suggesting that the single-waveguide effects continue. The resonances are eliminated in the band gaps and are also diminished when the 2D LDOS is low [Fig. 7(c)]. The individual cylinders also have resonances, but these affect both the finite and the infinite 2D PC's and thus are not a point of distinction between the two PC's. Nevertheless, they are relatively weak at the frequencies we consider.

The 2D MSPC cluster behaves like a low-index hexagonal dielectric waveguide in a high-index background. The hexagonal boundary makes quantifying the resonances difficult. However, we might expect them to be weak compared to those in the dielectric waveguide in air as the latter are bolstered by total internal reflection. This notion is supported by Figs. 7(e) and 7(f), where the 2D LDOS in the finite 2D

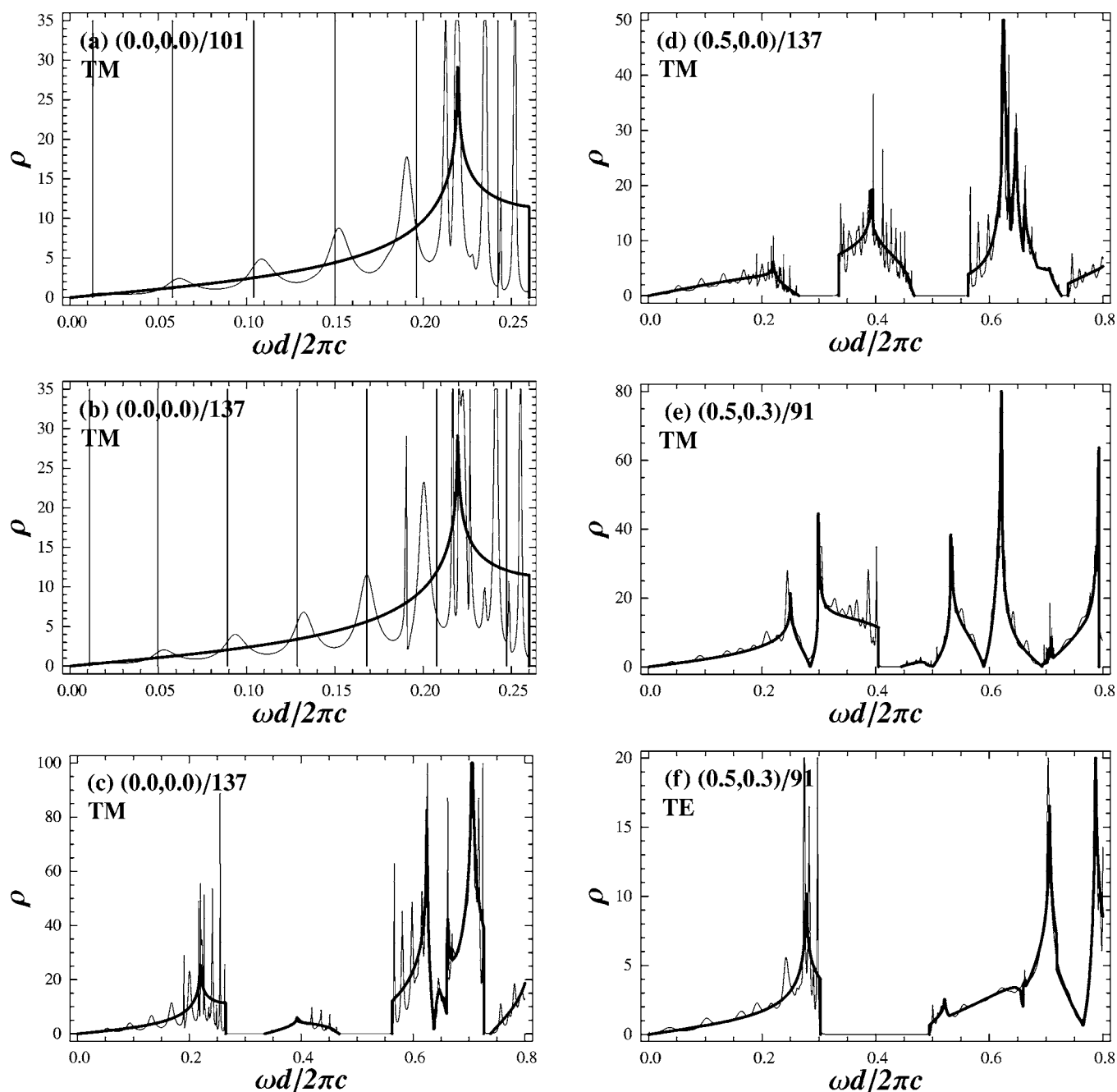


FIG. 7. 2D LDOS ρ in the 2D SQPC (a)–(d) and in the 2D MSPC (e) and (f) as infinite lattice (thick line) and as finite cluster (thin line). Cluster sizes: (a) $N_c=101$ cylinders, (b)–(d) $N_c=137$ cylinders, and (e)–(f) $N_c=91$ air voids. Vertical lines in (a) and (b) indicate waveguide resonances for the cluster in the homogenization limit.

PC follows that in the infinite 2D PC much more closely compared to Figs. 7(c) and 7(d).

The 2D LDOS in a finite 2D PC is therefore a superposition of two effects. The first is due to periodicity, which causes the 2D LDOS to trace the 2D LDOS in the infinite 2D PC. The second is due to resonances associated with the boundary of the periodic region, which causes the 2D LDOS to oscillate about the 2D LDOS in the infinite 2D PC. The size of the discrepancy between the finite and infinite PC's is thus determined by the strength of the resonances. In a 2D PC composed of dielectric cylinders like the 2D SQPC, the resonances are strong and the discrepancy is large.

V. DISCUSSION AND CONCLUSION

We have presented a comprehensive analysis of the 2D LDOS and level shift in 2D PC's. Crucial to obtaining accurate density of states functions was the Rayleigh-multipole method, which allowed us to obtain Bloch modes and Bloch functions to high accuracy. We demonstrated how the important features in the level shift, in addition to the 2D DOS, are interpreted using the 2D band structure through critical point analysis. We also related the 2D DOS to the 2D LDOS through Bloch functions. This analysis produced two notable results. First, as the level shift varies on the same scale as the

DOS and LDOS, the large variations in the DOS and LDOS that occur at critical points produce equally large variations in the level shift. Second, the significant band-edge jumps in the 2D DOS about a band gap produce peaks in the level shift with opposite signs, forcing the level shift to pass through zero inside the band gap. For the 2D LDOS by contrast, the band-edge jump on one side of the band gap is removed by the nodes of the Bloch functions, and the level shift instead passes through zero outside the band gap. Finally, we compared the 2D LDOS in infinite and finite 2D PC's. The two results differ by the strength of the resonances produced by the boundary of the finite 2D PC. In finite 2D PC's where the effective refractive index of the cluster is higher than the surrounding material, the resonances are very strong and produce a marked discrepancy.

While the fully 2D system we have considered here lacks general applications, it is practical for computational modeling and theoretical understanding. Note though that except for the critical point behavior, the above results are not dimensionally specific. Perhaps most importantly, we have reconciled the crucial quantity for radiation dynamics experiment in a PC—the LDOS in a finite PC—with the source of the basic physics of the PC—the band structure. We have also shown that level shifts in PC's are altered by a large and measurable extent by their environment. While considerably more challenging, repeating this analysis for 3D PC's would provide valuable insight into the novel radiation dynamics predicted in the fully 3D systems.

ACKNOWLEDGMENTS

This work was produced with the assistance of the Australian Research Council (ARC) under the ARC Centres of Excellence program. CUDOS (Center for Ultra-high bandwidth Devices for Optical Systems) is an ARC Centre of Excellence.

APPENDIX A: RAYLEIGH-MULTIPOLE METHOD

1. Formalism

We consider the two-dimensional diffraction problem of wave propagation in the plane of an infinite array of parallel dielectric cylinders. The cylinders are arranged in a Cartesian coordinate system with the cylinder axes aligned with the z axis and the lattice lying in the xy plane with lattice constant d . When the wave vector \mathbf{k} is confined to the xy plane, the transverse (to the z axis) magnetic (TM) and transverse electric (TE) fields decouple. The electromagnetic (EM) eigenvalue problem reduces to two scalar problems. The two independent solutions are obtained from the two-dimensional Helmholtz equation

$$\nabla^2 V(\mathbf{r}) + k^2 n(\mathbf{r})^2 V(\mathbf{r}) = 0, \quad (\text{A1})$$

where $k=2\pi/\lambda$ is the wave number and $n(\mathbf{r})$ is the positional refractive index. V is the z component of the field, with $V = \Psi_z^E$ for TM polarization and $V = \Psi_z^H$ for TE polarization.

We solve Eq. (A1) using the Rayleigh-multipole method [18]. The salient points are as follows. A Fourier-Bessel basis

is used to represent the field in the vicinity of the l th cylinder as

$$V_l(\mathbf{r}) = \sum_{n=-\infty}^{\infty} [A_n^l J_n(k|\mathbf{r} - \mathbf{R}_l|) + B_n^l H_n^{(1)}(k|\mathbf{r} - \mathbf{R}_l|)] e^{in \arg(\mathbf{r} - \mathbf{R}_l)}, \quad (\text{A2})$$

where J_n is a Bessel function of the first kind, $H_n^{(1)}$ is a Hankel function of the first kind, and A_n^l and B_n^l are the multipole coefficients. Equation (A2) is the local field expansion and applies in the annulus between the cylinder surface and the nearest external source. The global field expansion is derived by an application of Green's theorem to Eq. (A2) and applies everywhere outside the cylinders. The equality of the local and global field expansions is enforced using Graf's addition theorem. This results in an infinite system of linear equations $\mathbf{A} = \mathbf{S}\mathbf{B}$, linking vectors of the multipole coefficients $\mathbf{A} = [A_n]$ and $\mathbf{B} = [B_n]$ via a Toeplitz matrix \mathbf{S} of lattice sums. The lattice sums [33–36] can be computed rapidly, using a convergence test to determine the truncation term. This results in the elements of \mathbf{S} being determined close to machine precision.

A second connection between the multipole coefficients comes from enforcing the boundary conditions at the surface of the cylinder at the origin. This results in the vector equation $\mathbf{B} = \mathbf{R}\mathbf{A}$, where the polarization-dependent matrix \mathbf{R} gives the reflection coefficient in the multipole basis for a source located outside the cylinder [34–36]. Combining the two linear equations linking the vectors of multipole coefficients, we arrive at a matrix equation which may be used to find the modes of the lattice of cylinders:

$$[\mathbf{I} - \mathbf{R}\mathbf{S}]\mathbf{B} = \mathbf{M}\mathbf{B} = \mathbf{0}, \quad (\text{A3})$$

where \mathbf{I} is the matrix identity and the matrix $\mathbf{M} = \mathbf{M}(k, \mathbf{k}_0)$ is a function of frequency and the Bloch vector. While Eq. (A3) is not explicitly an eigenvalue equation, it embodies the eigenvalue problem of the infinite two-dimensional periodic array and the modes are given by the (k, \mathbf{k}_0) pairs at which

$$\det[\mathbf{M}(k, \mathbf{k}_0)] = 0. \quad (\text{A4})$$

Botten *et al.* reported an alternative approach to performing band-structure calculations in 2D PC's that is also based on the multipole method in a single grating [37]. In this approach, repetition in the second dimension is achieved using transfer-matrix methods in a Bloch-mode basis to combine the gratings in adjacent layers. The formulation yields an explicit eigenvalue problem, which is much more computationally efficient for mode finding than the current approach. However, when the cylinders of adjacent layers interpenetrate, as in a hexagonal lattice with cylinder radius $a/d > 0.4$, the method fails. While the current approach can be computationally cumbersome if the determinant varies rapidly about a mode, it is robust, and band structures can be obtained in any 2D PC composed of cylinders, as long as the cylinders do not overlap.

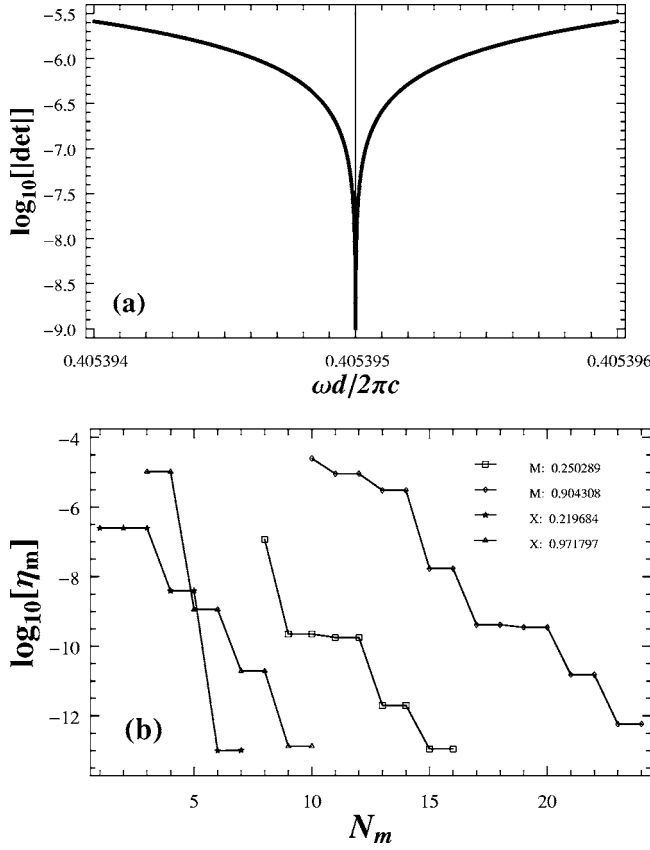


FIG. 8. (a) The determinant in 2D of the MSPC for TM polarization at the nondegenerate second mode of the Γ point [Fig. 1]. (b) Convergence testing where $\eta = |\omega_{N_m} - \omega_{N_m}^*| / |\omega_{N_m}^*|$ is the measure of convergence with respect to the truncation parameter N_m . Legend indicates frequency ($\omega d/2\pi c$) of 2D MSPC modes taken from the M point and 2D SQPC modes taken from the X point. For the 2D MSPC, $N_m^* = 32$, while for the 2D SQPC, $N_m^* = 13$.

2. Numerics

For a given Bloch vector \mathbf{k}_0 , the determinant in Eq. (A4) is a function of frequency (ω/c or k) only, and the modes ω_{l,\mathbf{k}_0} can be obtained at the zeros. The determinant is shown in Fig. 8(a). While $|\det[\mathbf{M}(k, \mathbf{k}_0)]|$ never actually vanishes, it has local minima at the modes that are effectively zeros. When $|\det[\mathbf{M}(k, \mathbf{k}_0)]|$ is evaluated on a logarithmic scale, the minima at the modes are sharp. This makes them distinct from other minima and allows them to be evaluated numerically with an accuracy close to machine precision [38]. The degeneracy can be determined through $\text{Re}\{\det[\mathbf{M}]\}$, which is an odd function of frequency about a nondegenerate mode and an even function about a doubly degenerate mode.

Once a mode has been found, the singular value decomposition (SVD) [38] of the \mathbf{M} matrix can be used to obtain the \mathbf{B} vector. While less computationally efficient, the degeneracy of a mode can also be determined from this SVD. The \mathbf{B} vector can then be used to obtain the \mathbf{A} vector using $\mathbf{A} = \mathbf{S}\mathbf{B}$ and thence the Bloch functions Ψ_{l,\mathbf{k}_0} through Eq. (A2).

The multipole sums in the field expansions (A2) are truncated to the terms $m = -N_m, \dots, N_m$, where N_m is the truncation parameter. The sums thus contain $2N_m + 1$ terms, and the

dimensions of the matrices in Eq. (A3) are $(2N_m + 1) \times (2N_m + 1)$. In Fig. 8(b) we demonstrate the convergence in the eigenfrequency of modes with respect to N_m . This is done at the M point in the BZ of the 2D MSPC and the X point in the BZ of the 2D SQPC. The convergence depends on two factors. First, multipole expansions converge more rapidly when the highest-order terms enter the large-order limit for Bessel functions [39]. This occurs when $N_m > M$ where M is the largest argument in the Bessel functions with $M \sim k \max(n_b, n_t)a$. The rate of convergence accordingly deteriorates, in general, with increasing frequency. Second, the number of multipole terms must be sufficient for the full symmetry and structure of a mode to be satisfied. Convergence in the hexagonal lattice with sixfold symmetry is thus much poorer than for the square lattice with fourfold symmetry. The first effect is relatively slow to set in, so it is the second effect that dominates, in general.

We apply our Rayleigh-multipole method to computing the band diagram formed by tracing the Bloch vector around the edge of the IBZ and the band surfaces formed by the Bloch vectors in the IBZ. This is done using an algorithm that minimizes the computationally expensive evaluation of $\det[\mathbf{M}]$. The minima must first be bracketed before being computed precisely. The initial search is performed at a low-symmetry point in the IBZ where the separation between the modes in adjacent bands is generally largest. This is the M point for the hexagonal lattice and the X point for the square lattice. The minima at this point are bracketed searching at equally spaced intervals of $\omega d/2\pi c = 10^{-4}$. The brackets for modes at adjacent points in the IBZ are then obtained by extrapolating from previously computed modes. We typically use 41 points on each side of the IBZ. While the curvature in bands varies, a cubic polynomial fit to four consecutive points typically yields an estimate with accuracy better than $\omega d/2\pi c = 10^{-6}$ for an adjacent point.

APPENDIX B: CALCULATION OF THE 2D DOS AND 2D LDOS

Several methods have been developed to compute the DOS and LDOS in solid-state physics. All methods sample the BZ with a discrete set of Bloch vectors and then use interpolation to evaluate the contour integrals in Eqs. (7) and (6) across the BZ. Due to its simplicity, the linear-tetrahedron (or triangle in 2D) method [40,41] has been the most widely adopted in solid-state physics and the sole method used for infinite PC's. However, it has two major deficiencies. First, linear interpolation is inadequate at van Hove singularities, which led to the quadratic method [42]. Second, the requirement to allocate bands introduces the band crossing problem, which led to extrapolative techniques over several bands [43,44]. Despite the greatly improved accuracy, these two more complex methods have not been widely implemented. Here, we adopt a method incorporating cubic B -splines which we believe is both computationally efficient and addresses the inadequacies of the linear-triangle method.

The band surfaces over the IBZ are formed on a discretized square grid. The particular IBZ used for the 2D MSPC is shown in the inset of Fig. 1 and for the 2D SQPC

in Fig. 4. The IBZ is overlaid on the grid so that it completely covers the upper-left right triangle of the grid. Using a square grid ensures that points on the Γ - M segment for the 2D SQPC and Γ - K for the 2D MSPC are captured. We generally find that using a grid with 41 points in the columns and rows offers the best compromise between minimizing computation time and maximizing accuracy. The Bloch modes and Bloch functions at each Bloch vector on the grid are first obtained using the Rayleigh-multipole method (see Appendix A). The band surfaces are then formed by ordering the mode frequencies at each Bloch vector and then allocating them to bands so that $l < l+1$ implies that $\omega_l(\mathbf{k}_0) \leq \omega_{l+1}(\mathbf{k}_0)$. As is well known, this is the only robust solution to the band ordering problem. A close inspection of Figs. 1 and 4 will attest that if we begin at a mode at the Γ point and then traverse the boundary of the IBZ, we are not guaranteed to return to the same mode if we allow bands to cross when they are connected at degeneracies.

The interpolation scheme we adopt uses univariate cubic B -splines [45] fitted to data in the rows, columns, and diagonal of the IBZ grid. For the l th band, the data consists of (i) the mode frequencies of the band surface $\omega_l(\mathbf{k}_0)$, (ii) the magnitude of the group velocity on $\omega_l(k_{0x}, k_{0y})$,

$$v_g = \sqrt{\left(\frac{\partial\omega_l}{\partial k_{0x}}\right)^2 + \left(\frac{\partial\omega_l}{\partial k_{0y}}\right)^2}, \quad (\text{B1})$$

and (iii) the field points of the Bloch function $\Psi_l(\mathbf{k}_0, \mathbf{r})$ covering the WSC, at each Bloch vector on the grid. All quantities required to evaluate the BZ integrals can be obtained from the careful use of the splines fitted to this data. Two fitting tasks are required to ensure the accuracy of the splines. First, the first derivatives at the ends of the splines must be given. As the ends lie on the boundary of the IBZ, these are easily obtained from symmetry arguments. Second, the first derivative is discontinuous at certain band connections noted above that might have been band crossings if not for the chosen band ordering. Fitting a smooth curve in this

case will yield inaccurate interpolation near the band connection. We overcome this problem by setting knots in the splines at these band connections. Accuracy is retained in the vicinity of these points, and while the derivatives remain undefined precisely at the connection, a contour at a discrete frequency is unlikely to encounter the connection.

The contours in each band are obtained at a discrete set of frequencies $\omega l/2\pi c = p\delta\omega$ where $p \in \mathbb{N}$. In our calculations we use $\delta\omega = 0.0005$. As the splines are composed piecewise of cubic polynomials, the intersection of the band surface splines and the contour frequencies can be obtained analytically. The partial derivatives in Eq. (B1) are also obtained analytically from the band-surface splines. At each grid point, $\partial\omega_l/\partial k_{0x}$ is obtained from the row splines, $\partial\omega_l/\partial k_{0y}$ from the column splines, and thus from Eq. (B1) the group velocity at each grid point. This grid is again fitted with univariate cubic splines from which the group velocity at every contour point can be obtained. Constructing contours from the contour points is straightforward. Smooth contours are obtained by fitting a cubic spline to the contour points, allowing the contour integral in Eq. (7) to be computed to high accuracy to give the 2D DOS.

The Bloch functions are computed along with the Bloch modes. The field points for both the 2D SQPC and 2D MSPC are obtained on a square grid. The boundary of the grid for the 2D SQPC is $0.5d$, while for the 2D MSPC it is extended to $0.6d$ to ensure that the WSC is covered. The field points are at $(x, y)d = (l_x, l_y)\delta xd$ where $(l_x, l_y) \in \mathbb{Z}^2$. In our calculations we use $\delta x = 0.05$. Similar again to the band surface, a square grid is constructed for each field point covering the IBZ and fitted with univariate splines. The field point at each contour point is obtained from the splines, and the contour integral in Eq. (6) is then computed for each field point. Completing this for each field point in the unit cell gives the $i=1$ element of the sum in Eq. (6). This surface is then fitted with a bivariate spline [45] and the other elements of the sum are obtained by the point-group operations. Finally, the sum in Eq. (6) is evaluated to give the 2D LDOS.

-
- [1] E. Yablonovitch, Phys. Rev. Lett. **58**, 2059 (1987).
 [2] S. John, Phys. Rev. Lett. **58**, 2486 (1987).
 [3] J. D. Joannopoulos, R. D. Meade, and J. N. Winn, *Photonic Crystals: Molding the Flow of Light* (Princeton University Press, Princeton, NJ, 1995).
 [4] S. Haroche and D. Kleppner, Phys. Today **42**(1), 24 (1989); *Cavity Quantum Electrodynamics*, edited by P. Berman (Academic Press, New York, 1994); E. A. Hinds, in *Advances in Atomic, Molecular and Optical Physics*, edited by Sir D. Bates and B. Bederson (Academic Press, New York, 1991).
 [5] S. John and J. Wang, Phys. Rev. Lett. **64**, 2418 (1990).
 [6] A. G. Kofman, G. Kurizki, and B. Sherman, J. Mod. Opt. **41**, 353 (1994).
 [7] N. Vats, S. John, and K. Busch, Phys. Rev. A **65**, 043808 (2002).
 [8] F. Bassani and G. Pastori Parravicini, *Electronic States and Optical Transitions in Solids* (Pergamon Press, London, 1975).
 [9] R. Sprik, B. A. van Tiggelen, and A. Lagendijk, Europhys. Lett. **35**, 265 (1996).
 [10] K.-M. Ho, C. T. Chan, and C. M. Soukoulis, Phys. Rev. Lett. **65**, 3152 (1990).
 [11] K. Busch and S. John, Phys. Rev. E **58**, 3896 (1998).
 [12] J. M. Pottage, D. M. Bird, T. D. Hedley, T. A. Birks, J. C. Knight, and P. St. J. Russell, Opt. Express **11**, 2854 (2003).
 [13] Z.-Y. Li, L.-L. Lin, and Z.-Q. Zhang, Phys. Rev. Lett. **84**, 4341 (2000).
 [14] X.-H. Wang, B.-Y. Gu, R. Wang, and H.-Q. Xu, Phys. Rev. Lett. **91**, 113904 (2003).
 [15] V. Lousse, J.-P. Vigneron, X. Bouju, and J.-M. Vigoureux, Phys. Rev. B **64**, 201104 (2001).
 [16] Z.-H. Li and Y. Xia, Phys. Rev. B **63**, 121305 (2001).
 [17] X.-H. Wang, Y. S. Kivshar, and B.-Y. Gu, Phys. Rev. Lett. **93**, 073901 (2004).
 [18] R. C. McPhedran, N. A. Nicorovici, L. C. Botten, and Ke-Da

- Bao, in *Wave Propagation in Complex Media*, edited by G. Papanicolaou, IMA Volumes in Mathematics and its Applications (Springer-Verlag, New York, 1998), Vol. 96, p. 155.
- [19] R. C. McPhedran, L. C. Botten, J. McOrist, A. A. Asatryan, C. Martijn de Sterke, and N. A. Nicorovici, *Phys. Rev. E* **69**, 016609 (2004).
- [20] A. A. Asatryan, K. Busch, R. C. McPhedran, L. C. Botten, C. Martijn de Sterke, and N. A. Nicorovici, *Phys. Rev. E* **63**, 046612 (2001); *Opt. Express* **8**, 191 (2001).
- [21] D. P. Fussell, R. C. McPhedran, C. Martijn de Sterke, and A. A. Asatryan, *Phys. Rev. E* **67**, 045601(R) (2003); D. P. Fussell, R. C. McPhedran, and C. Martijn de Sterke, *ibid.* **70**, 066608 (2004).
- [22] P. Lambropoulos, G. M. Nikolopoulos, T. R. Nielsen, and S. Bay, *Rep. Prog. Phys.* **63**, 455 (2000).
- [23] X.-H. Wang, B.-Y. Gan, and R.-Z. Wang, *Phys. Lett. A* **308**, 116 (2003).
- [24] D. P. Fussell, R. C. McPhedran, and C. Martijn de Sterke, *Phys. Rev. A* **71**, 013815 (2005).
- [25] R. N. Bracewell, *The Fourier Transform and its Applications*. 3rd ed. (McGraw-Hill, New York, 2000), pp. 359–366.
- [26] J. Callaway, *Quantum Theory of the Solid State* (Academic, New York, 1974).
- [27] M. Morse, *Am. Math. Monthly* **49**, 358 (1942).
- [28] L. van Hove, *Phys. Rev.* **89**, 1189 (1953).
- [29] J. C. Phillips, *Phys. Rev.* **104**, 1263 (1956).
- [30] U. Gruning, V. Lehmann, and C. M. Engelhardt, *Appl. Phys. Lett.* **68**, 747 (1996); J. Schilling, R. B. Wehrspohn, A. Birner, F. Muller, R. Hillebrand, U. Gosele, S. W. Leonard, J. P. Mondia, F. Genereux, H. M. van Driel, P. Kramper, V. Sandoghdar, and K. Busch, *J. Opt. A, Pure Appl. Opt.* **3**, S121 (2001).
- [31] H. Bethe, *Phys. Rev.* **72**, 339 (1947).
- [32] G. W. Milton, *The Theory of Composites* (Cambridge University Press, Cambridge, England, 2001).
- [33] R. C. McPhedran, N. A. Nicorovici, L. C. Botten, and K. A. Grubits, *J. Math. Phys.* **41**, 7808 (2000).
- [34] V. Twersky, *Arch. Ration. Mech. Anal.* **8**, 323 (1961).
- [35] L. C. Botten, N. A. Nicorovici, A. A. Asatryan, R. C. McPhedran, C. M. de Sterke, and P. A. Robinson, *J. Opt. Soc. Am. A* **17**, 2165 (2000).
- [36] N. A. Nicorovici, R. C. McPhedran, and R. Petit, *Phys. Rev. E* **49**, 4563 (1994).
- [37] L. C. Botten, N. A. Nicorovici, R. C. McPhedran, C. M. de Sterke, and A. A. Asatryan, *Phys. Rev. E* **64**, 046603 (2001).
- [38] W. H. Press, S. A. Teukolsky, W. T. Vetterling, and B. P. Flannery, *Numerical Recipes in Fortran: The Art of Scientific Computing* (Cambridge University Press, Cambridge, England, 1996).
- [39] *Handbook of Mathematical Functions*, edited by M. Abramowitz and I. A. Stegun (Dover, New York, 1972).
- [40] G. Lehmann and M. Taut, *Phys. Status Solidi B* **54**, 469 (1972).
- [41] J. Hanna, M. Watanabe, and T. Kato, *J. Phys.: Condens. Matter* **2**, 7445 (1990).
- [42] M. S. Methfessel, M. H. Boon, and F. M. Mueller, *J. Phys. C* **16**, L949 (1983).
- [43] J. E. Muller and J. W. Wilkins, *Phys. Rev. B* **29**, 4331 (1984).
- [44] C. J. Pickard and M. C. Payne, *Phys. Rev. B* **59**, 4685 (1999).
- [45] P. Dierckx, *Curve and Surface Fitting with Splines* (Oxford University Press, Oxford, 1993); <http://netlib.org/dierckx/>.